AGU PUBLICATIONS

JGR

Journal of Geophysical Research: Space Physics

RESEARCH ARTICLE

10.1002/2014JA020632

**Key Points:**
- Model substorm precipitation is validated with ground-based observations
- All four types of riometer spike event emerge in the model results
- Model can predict precipitation hours after a substorm onset is detected

**Correspondence to:**
M. J. Beharrell,
m.beharrell@lancaster.ac.uk

**Citation:**
Beharrell, M. J., F. Honary, C. J. Rodger, and M. A. Clilverd (2015), Substorm-induced energetic electron precipitation: Morphology and prediction, *J. Geophys. Res. Space Physics*, *120*, 2993–3008, doi:10.1002/2014JA020632.

Received 18 SEP 2014
Accepted 20 FEB 2015
Accepted article online 25 FEB 2015
Published online 6 APR 2015



# Substorm-induced energetic electron precipitation: Morphology and prediction

**M. J. Beharrell[1], F. Honary[1], C. J. Rodger[2], and M. A. Clilverd[3]**

[1]Physics Department, Lancaster University, Lancaster, UK, [2]Department of Physics, University of Otago, Dunedin, New Zealand, [3]British Antarctic Survey, Cambridge, UK

**Abstract** The injection, and subsequent precipitation, of 20 to 300 keV electrons during substorms is modeled using parameters of a typical substorm found in the literature. When combined with onset timing from, for example, the SuperMAG substorm database, or the Minimal Substorm Model, it may be used to calculate substorm contributions to energetic electron precipitation in atmospheric chemistry and climate models. Here the results are compared to ground-based data from the Imaging Riometer for Ionospheric Studies riometer in Kilpisjärvi, Finland, and the narrowband subionospheric VLF receiver at Sodankylä, Finland. Qualitatively, the model reproduces the observations well when only onset timing from the SuperMAG network of magnetometers is used as an input and is capable of reproducing all four categories of substorm associated riometer spike events. The results suggest that the different types of spike event are the same phenomena observed at different locations, with each type emerging from the model results at a different local time, relative to the center of the injection region. The model's ability to reproduce the morphology of spike events more accurately than previous models is attributed to the injection of energetic electrons being concentrated specifically in the regions undergoing dipolarization, instead of uniformly across a single-injection region.

## 1. Introduction

The accurate modeling of medium-energy particle precipitation (20 keV to 1 MeV), and the corresponding absorption measured by a riometer, has long been considered a very difficult problem [see, e.g., *Hargreaves*, 2007]. A significant contributor to this difficulty is the irregularity and unpredictability of substorms, which provide a significant proportion of precipitating electrons in the relevant energy range (> 20 keV). The mesospheric effects of medium-energy electron precipitation have been modeled by *Codrescu et al.* [1997] and found to produce significant increases in $n_e$, $HO_X$, $NO_2$, and NO, along with significant decreases in $O_3$ between 70 and 80 km in the polar regions. The implications for climate science are clear, but there are currently no studies of the effects of individual substorms on mesospheric composition. The aim of this work is to provide a model of the medium-energy electron precipitation produced by substorms, which may be used as a driver in climate models, or for predicting *D* region ionospheric conditions in the short term (minutes to hours) following a detected substorm onset.

The substorm cycle consists of three phases: growth, expansion, and recovery [*Akasofu*, 1964]. In the growth phase energy gradually accumulates in the magnetosphere. This energy is rapidly released during the expansion phase, so named because a brightening of the aurora, which typically begins at 23.5 ± 2 h magnetic local time [*Nagai*, 1991], expands in latitude and local time.

During expansion, which lasts around 0.5 h, the tail of the magnetosphere returns to a more dipolar configuration. The changing magnetic field accelerates electrons and ions to energies of up to a few hundred keV, while injecting them from the tail into trapped orbits closer to the Earth. These energies are too low for significant numbers of the ions, which are mostly protons, to reach the *D* region or lower *E* region of the ionosphere, where absorption measured by riometers occurs. The rapid relaxation of the magnetic field allows ground magnetometers to detect the onset of substorm expansion from deviations in the H component of the field. A list of magnetometer-detected substorm onset times is compiled and published by the SuperMAG collaborators [*Newell and Gjerloev*, 2011]. This list will be used in our study for the timing of electron injections that accompany substorm expansion.

The exact process and order of events leading to onset and expansion are still hotly contested. Many recent publications present evidence in support of an "outside-in" paradigm, in which substorms are initiated by reconnection in the tail, generating earthward flow of plasma [see, e.g., *Angelopoulos*, 2008; *Birn*, 2011, and references therein]. In this picture dipolarization can be viewed as the piling up of magnetic flux caused by the breaking of this flow. However, a number of other recent publications conclude consistency with an "inside-out" model, known as the Current Disruption Model, in which the substorm is assumed to be triggered by a current-driven instability at 8 to 10 $R_E$. The resulting diversion of current, known as the substorm current wedge, grows over time, dipolarizing the magnetotail, and injecting energized particles into the nightside magnetosphere.

Several previous studies have attempted to model the substorm injection process physically. *Sarris et al.* [2002] considered an earthward propagating electromagnetic pulse, which interacts with a preexisting electron population. *Kim et al.* [2000] and *Liang et al.* [2007] traced electrons in a guiding center approach, in realistic magnetic fields. When the magnetic field changes imparted by dipolarization are neglected, these models are still capable of adequately describing the properties of dispersed injections [*Gabrielse et al.*, 2012]. However, the models described in *Kabin et al.* [2011] and *Zaharia et al.* [2004] include time-dependent magnetic fields, i.e., they include betatron acceleration from the dipolarization. The changing magnetic field imparts significantly more acceleration to the electrons than transportation alone. *Kabin et al.* [2011] argues that dispersionless injections could even be explained by local betatron acceleration alone, without additional particle transport.

The model of *Liang et al.* [2007] gives reasonable values for electron precipitation flux, (integrated over energies > 30 keV,) and is capable of producing precipitation signatures similar to those of some spike events observed by ground-based riometers. Spike events are sudden increases in ionospheric absorption in riometer data that were first studied by *Parthasarathy and Berkey* [1965]. Spikes occurring in the dayside ionosphere have been connected to Magnetic Impulse Events [*Terkildsen et al.*, 2001], whereas nighttime events are strongly associated with substorms, and are generally more intense. Each substorm onset and/or breakup may be accompanied by a spike event [*Aminaei et al.*, 2006].

Global MHD simulations have provided some encouraging results when reproducing substorm observations [*Lyon et al.*, 1998; *Raeder et al.*, 2008]. However, some questions remain about the validity of the approximations they use, in particular whether a numerical resistivity procedure for substorm initiation corresponds to a real physical process [*Lui*, 2007].

*Clilverd et al.* [2008] studied the ionospheric effects of substorm injections using ground-based subionospheric VLF and riometer observations, in tandem with measurements of electron flux made by the spacecraft LANL-97A. Comparing the ground-based observations and satellite measurements, they were able to estimate that between 50% and 70% of the LANL-97A measured electron flux was precipitating into the ionosphere.

In section 2, we describe the substorm injection process, as outlined by *Kennel* [1995] and provide a mathematical description of the medium electron precipitation following such a process. The results, calculated with onset timing from the SuperMAG substorm database, are then compared with measurements from ground-based instruments in an attempt to determine the validity of the process. A description of the model is given in section 3, along with the parameter values chosen and the reasons for each choice. In section 4 we present the results of the model, some comparisons with ground-based observations, and show the ability of the model to reproduce each category of nightside spike event commonly observed in riometer data.

## 2. The Substorm Injection Process

During the growth phase of a substorm, the magnetic field near the inner edge of the cross-tail current sheet becomes more tail like, i.e., stretched away from the planet. At onset, dipolarization starts in a small region surrounding the central meridian. The initial size of this region is localized to 1 $R_E$ or less [*Ohtani et al.*, 1991] at geostationary distance. As time passes, the dipolarization front propagates eastward and westward, accompanied by dispersionless injections of particles [*Kennel*, 1995]. Outside this region the magnetic field remains stretched in a tail-like configuration, whereas inside the region it has returned to a more dipolar shape.

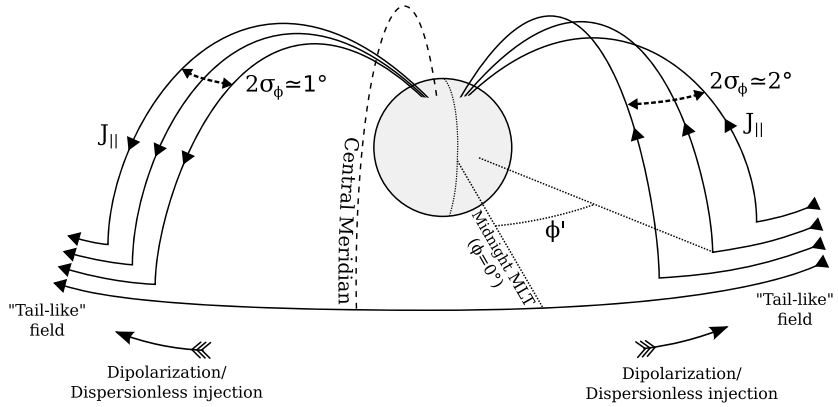


**Figure 1.** The substorm current wedge and injection process [after *Kennel*, 1995].

The exact mechanism responsible for the injection of medium-energy (tens to hundreds of keV) electrons at the dipolarization front is still uncertain. *Li et al.* [1998] argues that electrons are energized by betatron acceleration, whereas *Sarafopoulus* [2008] proposes a mechanism based on the accumulation of charge at the sharp tip of the stretched field lines. However, it is clear that the injection mechanism is distinct from those producing lower energy (<10 keV) auroral electrons. The different mechanisms appear to operate in different spatial regions, at different times, and at different energies. For example, electrons of tens of keV or greater that are injected at the western edge of the substorm current wedge can drift eastward across the activation region without further acceleration [*Lazutin et al.*, 2007], whereas lower energy auroral electrons will gain much structure from mechanisms that are as varied as the diverse forms of aurora. It is the more energetic population of electrons (20 keV to 300 keV) that are modeled herein. These precipitate to low altitudes of the ionosphere, where they are responsible for increased absorption, measured by riometers, and variations in the signals received from subionospherically propatating VLF waves [*Rodger et al.*, 2012].

## 3. Model Description

Some simplifying assumptions are made in the mathematical representation of the injection process, namely, the dispersionless injection spectrum is fixed over the duration of the injection, the expansion of the substorm current wedge occurs at a constant rate, and the electrons drift on fixed L shells. Additionally, the loss rate of electrons to precipitation and their drift velocities are assumed to be functions of their energy, but independent of time. In the current study, neither an outside-in nor an inside-out order is assumed; instead, the substorm injection timing is independent of magnetic latitude.

The aim is to produce, as far as is possible, a set of straightforward analytic expressions for calculating substorm-induced electron precipitation, in terms of measurable physical parameters. In cases where estimates of precipitating electron fluxes can be made from multiple observations, such as with a chain of riometers, it will be possible to fit the expressions to the measurements, thereby obtaining physical parameters of individual substorms. In the following sections we describe the parameters to be used in the model and identify typical values for each of them.

### 3.1. Azimutal Location of Injection

The injection of energetic electrons is closely associated with the regions of dipolarization and field-aligned currents, at the edges of the substorm current wedge [*Lopez et al.*, 1989]. Initially, the upward and downward field-aligned currents are close to the central meridian, but they do not overlap; see Figure 1. *Ohtani et al.* [1991] gives a value of $\leq 1\ R_E$ for the initial separation at $L = 6\ R_E$, this translates to an azimuthal angle of ≤10°.

Azimuthal locations, $\phi$, in the model are defined in magnetic coordinates, with the origin at magnetic midnight. They are equivalent to magnetic local time but measured in degrees instead of hours. The central meridian is typically located at an azimuth of around $\phi_{CM} = -7.5°$ (i.e., 23.5 magnetic local time (MLT)). A range of 23.5 ± 1 MLT is given by *Nagai* [1991], whereas *Arnoldy and Moore* [1983] report that dipolarization begins within about 2 h local time of 2300 MLT, although occasionally the central meridian can be found much farther away.

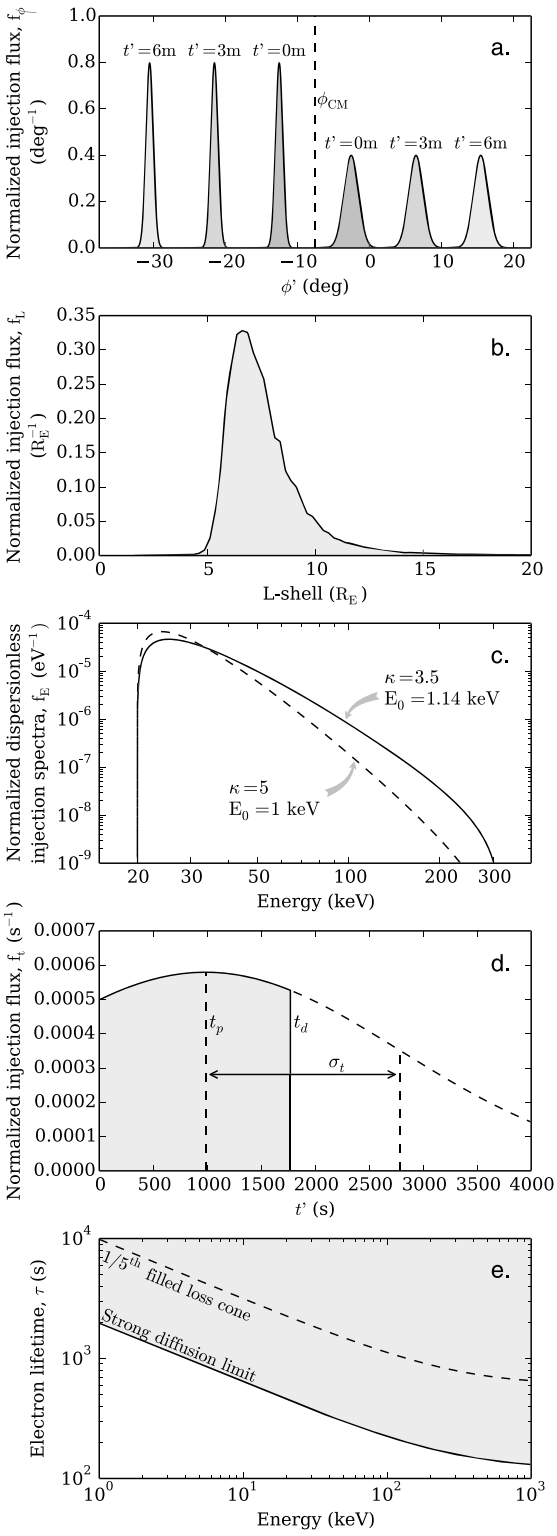


**Figure 2.** Parameters for a typical substorm: (a) $f_\phi$, the azimuthal location of the injection as a function of time; (b) $f_L$, the injection flux as a function of L shell; (c) $f_E$, the dispersionless injection spectrum; (d) $f_t$, the injection flux as a function of time; and (e) $\tau$, the mean lifetime of injected electrons as a function of energy, at $L = 6$.

Following onset, the dipolarization region expands eastward and westward with angular velocities of around 3°/min. Values in the literature include the following: 0.6°/min [*Atkinson*, 1972], 2°/min [*Kokobun and McPherron*, 1981], 5°/min to 15°/min [*Nagai*, 1982], and 3.5°/min (westward) and 4.8°/min (eastward) [*Nagai*, 1991]. With the assumption that this velocity is constant, the azimuthal positions of the east and west injection regions during a typical substorm are given by

$$\phi_{\text{east}}(t') = -7.5 + 5 + \frac{3}{60}t' \quad (^\circ) \qquad (1)$$

$$\phi_{\text{west}}(t') = -7.5 - 5 - \frac{3}{60}t' \quad (^\circ) \qquad (2)$$

where $t'$ is the number of seconds since substorm onset, −7.5° is the typical location of the central meridian, and ±5° provides the initial azimuthal separation of 10°.

The spatial sizes of the injection regions were inferred by *Robert et al.* [1984], who estimated their radii to be from 20 km to 900 km at geosynchronous orbit. This was achieved by measuring the width of the current filaments associated with substorm dipolarizations as they propagated across GOES 2. We use Gaussian distributions to represent the injection as a function of azimuth. Since a more distributed current connects to the ionosphere on the eastern edge compared to that on the western edge [*Kennel*, 1995], the Gaussian distributions are given standard deviations, $\sigma_\phi$, of 0.5° for the western injection region and 1° for the eastern region, consistent with the sizes inferred by *Robert et al.* [1984]. These values are illustrated in Figure 1. Normalized azimuthal distributions of the injections, $f_\phi$, which are centered on $\phi_{\text{east}}$ and $\phi_{\text{west}}$ (equations (1) and (2)), are shown in Figure 2a.

### 3.2. Distribution in L shell

The injection flux as a function of L shell, $f_L$, used in this study is given in Figure 2b. It is taken from *Cresswell-Moorcock et al.* [2013], who performed a reexamination of the L shell limits of energetic electron precipitation during substorms, using data from multiple low-Earth orbiting spacecraft.

### 3.3. Dispersionless Injection Spectra

The spectrum of the dispersionless injection, $f_W$, is assumed to be a kappa distribution; see Figure 2c. The kappa distribution is given by

$$f_E = \left(\frac{m_e}{2\pi\kappa E_0}\right)^{3/2} \frac{\Gamma(\kappa+1)}{\Gamma(\kappa-1/2)} \left(1+\frac{E}{\kappa E_0}\right)^{-\kappa-1} \tag{3}$$

The background plasma sheet electron distribution can be represented with values of $\kappa = 5$ and $E_0 = 1$ keV [*Liang et al.*, 2007]. For a typical substorm injection spectrum we use values from *Kim et al.* [2000] of $\kappa = 3.5$ and $E_0 = 1.14$ keV, which are based on measurements by *Christon et al.* [1991]. The difference between this spectrum and the power law used by *Clilverd et al.* [2008] for substorm-injected electrons is negligible over the energy range of interest. An upper energy limit to the dispersionless injection is reasonably well established, with only 20% of events energizing electrons to energies greater than 300 keV [*Baker et al.*, 1979]. Values for a lower energy limit include 10 keV [*Baker et al.*, 1989], 20 keV [*Lazutin et al.*, 2007], and 50 keV [*Reeves*, 1998]. For the case of a typical substorm, we therefore limit the spectrum to energies between 20 keV and 300 keV, with smooth cutoffs.

### 3.4. Time Evolution of Injection

The time variation of the injection flux, $f_t$ is assumed to be a Gaussian distribution, with width $\sigma_t$ and peak flux occurring at time $t_p$, as shown in Figure 2d. The injection ceases when the dipolarization reaches the flanks of the magnetosphere, at $t_d$ seconds after onset. At this time the dipolarization of the magnetospheric tail is assumed to be complete. A relatively flat distribution, peaking at the time of maximum current in the associated substorm current wedge, typically 16.4 min post onset [*Vagina and Sergeev*, 1996], was found to provide qualitatively good results.

### 3.5. Magnitude of Injection

So far, we have described an injection in terms of normalized density functions. These must be multiplied by the total number of injected electrons, $N_T$. This is the total number of energetic electrons that are injected over the course of a typical substom, and then precipitated into the atmosphere. The number is of the order $10^{28}$ [*Atkinson*, 1972]. In section 4 the value of $N_T$ is determined for 61 substorms by fitting the model to IRIS riometer observations. The fitted $N_T$ have a mean of $1.15 \times 10^{28}$ electrons, very close to the value of $10^{28}$ from *Atkinson* [1972]. With the duration of a typical substorm, $t_d$, being 1800 s (30 min), this translates to an average electron flux of $0.64 \times 10^{25}$ s$^{-1}$, not far from the rate of electron acceleration of $1 \times 10^{25}$ s$^{-1}$ to $4 \times 10^{25}$ s$^{-1}$ determined by *Atkinson* [1984].

### 3.6. Azimuthal Drift and Lifetime of Electrons

Following the injection, electrons drift eastward around the planet, with a drift velocity $\omega_d$. Although the electron energy spectrum throughout the injection is assumed to be constant, i.e., a dispersionless injection, the higher-energy electrons have higher drift velocities, traveling around the planet in a shorter time. This causes dispersion in the particle populations, which increases as the particles drift farther around the planet.

In degrees of magnetic longitude per second, the bounce-averaged drift velocity of electrons in a dipole field can be written as

$$\langle\omega_d\rangle = \frac{3LE}{22\times10^6}\left(0.7+0.3\sin\alpha_0\right) + 4.17\times10^{-3}, \tag{4}$$

[see, e.g., *Northrop*, 1966] where $L$ is measured in $R_E$, the energy $E$ in eV, and $\alpha_0$ is the equatorial pitch angle. The value $4.17 \times 10^{-3}$ is the contribution from Earth's rotation, since the magnetic field lines rotate with the Earth.

According to equation (4) the drift velocity of individual electrons will depend on their equatorial pitch angle, which suggests there will be an additional dispersion in the electron population, with high pitch angle particles drifting at higher rates. However, over a period of time corresponding to the pitch angle diffusion timescale, the electrons will share a similar average pitch angle, and the pitch angle dispersion will be reduced. For simplicity we use a single value for equatorial pitch angle, 39.5°, the average pitch angle in an isotropic distribution.

An electron that is injected $t'$ seconds after onset, at an azimuthal location $\phi'$, will reach the location $\phi$ at a time given by

$$t = \frac{\phi - \phi'}{\langle \omega_d \rangle} + t'. \tag{5}$$

The injected electrons drift toward the morning side, and when their fluxes reach the stably trapped limit [*Kennel and Petschek*, 1966] the pitch angle distribution of electrons with energies of tens of keV approaches isotropy, and their precipitation rate nears the strong diffusion limit [*Kennel*, 1969]. At this limit the proportion of particles precipitating into the ionosphere approaches a maximum value that depends on the size of the loss cone. For electrons with a bounce period of $T_B$ seconds, the lifetime in the strong diffusion regime is

$$\tau_{SD} \approx T_B L^3. \tag{6}$$

*Kennel and Petschek* [1966]. As a function of energy, $E$, and L shell, the electron bounce period in a dipole magnetic field is

$$T_B = \frac{LR_E}{c}\sqrt{\frac{m_e}{E}}\left(3.7 - 1.6\sin\alpha_0\right) \quad \text{(s)} \tag{7}$$

[e.g., *Baumjohann and Treumann*, 1996]. The electron rest mass (511 keV) is represented by $m_e$.

The primary mechanism by which electrons with energies greater than 20 keV are scattered into the loss cone, during all geomagnetic activities, is by interactions with lower band chorus waves [*Ni et al.*, 2011]. These are present more than 10% of the time and can persist during times of low geomagnetic activity [*Li et al.*, 2009].

Calculations by *Ni et al.* [2011] show that the bounce-averaged rates of pitch angle diffusion into the loss cone for 20 keV electrons reach the strong diffusion limit during geomagnetically active times ($AE > 300$ nT), and are approximately 1 order of magnitude below the limit in periods of moderate activity (100 nT $< AE <$ 300 nT). During substorms, an increased $AE$ index is observed, with values reaching up to 1000 nT during the April 2007 events that are presented in the following sections.

Based on the duration of riometer absorption events, *Liu et al.* [2007] argue that pitch angle diffusion of medium-energy electrons is likely to be close to the strong limit during substorms, with a timescale of $\tau \sim 1200$ s for the precipitation loss of 50 keV electrons at $L = 10\ R_E$. Applying constant strong diffusion in the model produces too much precipitation on the nightside, and too little on the dayside, but reducing the precipitation rate to one fifth of the strong diffusion limit is found to give acceptable results, with model precipitation levels on the dayside and nightside more closely matching observations of cosmic noise absorption during substorms. This is broadly similar to the diffusion rates used by *Liang et al.* [2007], who assume characteristic diffusion timescales of $D_{\alpha\alpha}^{-1} = 10$ s for substorm-injected electrons with bounce periods on the order of a few seconds.

Figure 2e shows the mean lifetime of electrons, $\tau$, as a function of energy, at $L = 6$. The solid line represents the strong diffusion limit, and the dotted line is the mean lifetime with the partially filled loss cone used throughout this study.

At $t$ seconds after onset, the proportion of electrons remaining, of those that were injected at $t'$ seconds after onset is

$$\delta = \exp\left[-(t - t')/\tau\right] \ . \tag{8}$$

### 3.7. Magnetospheric Density of Injected Electrons

To calculate the magnetospheric density of electrons along a field line, $N$ (in units of $\text{deg}^{-1}\ R_E^{-1}\ \text{eV}^{-1}$), at azimuth $\phi$, and $t$ seconds since onset, we sum over all injected electrons that reach $\phi$ at time $t$. Some of these electrons will be injected at an azimuth closer to $\phi$ than other electrons of the same energy but at a later time. The summation is equivalent to the following integration.

$$N = N_T\, f_E\, f_L \int_{t'=0}^{T} \delta(t')\, f_\phi(\phi'(t'))\, f_t(t')\ \mathrm{d}t' \tag{9}$$

where $f_E$, $f_L$, $f_\phi$, $f_t$ are the normalized distributions of the energetic electron injection in terms of energy (eV), L shell ($R_E$), azimuth (deg), and time since onset (s), respectively. $\phi'$ and $t'$ are dummy variables that do not appear in the solution to the integral. Electrons that were injected $t'$ seconds after the substorm onset, at the location $\phi'$, will drift to the location of the result, $\phi$ at time $t$. Rearranging equation (5) provides $\phi'(t')$ is found. $T$ is the smaller of the two values $t$ and $t_d$, which are the time since onset and the duration of the injection, respectively.

Representing $f_t$ and $f_\phi$ with Gaussian distributions allows the integral to be solved analytically. There are no such restrictions for the distributions in energy, $f_E$, and L shell, $f_L$, which are not inside the integral. The exact forms of each of the normalized distributions used in the model are shown in Figure 2. The solution to equation (9) is

$$\begin{aligned} N = {} & N_T f_E f_L \sqrt{\frac{1}{\pi Z}} \exp\left(\frac{X}{Z}\right) \\ & \times \left[\operatorname{erf}\left(\frac{t_p}{\sqrt{2}\sigma_t}\right) - \operatorname{erf}\left(\frac{t_p - t_d}{\sqrt{2}\sigma_t}\right)\right] \\ & \times \left[\operatorname{erf}\left(\frac{Y + (\sigma_\phi^2 + \sigma_t^2(\omega_d - \omega_i)^2)T}{\sigma_t \sigma_\phi \sqrt{Z}}\right)\right. \\ & \left. -\operatorname{erf}\left(\frac{Y}{\sigma_t \sigma_\phi \sqrt{Z}}\right)\right] \end{aligned} \tag{10}$$

where

$$\begin{aligned} X = {} & 2\omega_d {t_p}^2 \omega_i - {t_p}^2 {\omega_i}^2 - 2{\sigma_t}^2 t {\omega_i}^2/\tau + 2{\sigma_\phi}^2 t_p/\tau \\ & - 2\sigma_\phi^2 t/\tau - 2\omega_d t t_p \omega_i - 2\phi_{\mathrm{CM}} t_p \omega_i + 2\phi t_p \omega_i - \phi^2 \\ & + 2{\sigma_t}^2 \omega_d t \omega_i/\tau - 2{\sigma_t}^2 \phi_{\mathrm{CM}} \omega_i/\tau + 2{\sigma_t}^2 \phi \omega_i/\tau \\ & - {\omega_d}^2 {t_p}^2 + 2{\omega_d}^2 t_p t + 2\phi\phi_{\mathrm{CM}} - 2\omega_d \phi t_p + {\sigma_t}^2 {\sigma_\phi}^2/\tau^2 \\ & + 2{\sigma_t}^2 \omega_d \phi_{\mathrm{CM}}/\tau + 2\omega_d \phi_{\mathrm{CM}} t_p - {\phi_{\mathrm{CM}}}^2 - 2{\sigma_t}^2 \omega_d \phi/\tau \\ & - {\omega_d}^2 t^2 - 2\omega_d \phi_{\mathrm{CM}} t + 2\omega_d \phi t \\ Y = {} & {\sigma_t}^2 \left(\omega_d \phi - \phi \omega_i - {\sigma_\phi}^2/\tau + (\omega_i - \omega_d)(\omega_d t + \phi_{\mathrm{CM}})\right) \\ & - {\sigma_\phi}^2 t_p \\ Z = {} & 2\sigma_\phi^2 + 2\sigma_t^2 (\omega_d - \omega_i)^2 \end{aligned}$$

The variables and their values in the model are as follows. Reasons for these choices are given in sections 3.1 to 3.5. $\omega_d$ ($^\circ$ s$^{-1}$) is the azimuthal drift velocity of electrons, from equation (4). The azimuthal drift velocity of electrons is represented by $\omega_d$($^\circ$ s$^{-1}$); $\omega_i = \pm 0.05$ s$^{-1}$ is the azimuthal velocity of dipolarization; $\phi$ (degrees) is the azimuthal location of the result; $\phi_{\mathrm{CM}} = -7.5^\circ$ is the azimuthal location of the central meridian; $\sigma_\phi = 0.5^\circ$ (western injection) or 1° (eastern injection) is the azimuthal width of the injection; $t$ (s) is the time since substorm onset, which is determined using the onset times in the SuperMAG substorm database; $t_p = 984$ s is the time of peak injection flux during each substorm; $\sigma_t = 1800$ s is the temporal width of the injection; $\tau$ (s) is the mean lifetime of electrons before they are lost to precipitation, a value of $5\tau_{\mathrm{SD}}$ is assumed for the reasons discussed in section 3.6; and $\tau_{\mathrm{SD}}$ is given by equation (6).

Equation (10) is calculated for a number of electron energy values (~300, log spaced) in the range 20 keV to 300 keV and for each injection occurring in the preceding 12 h. It is possible to use different values for the parameters of each particle injection, and this is the case for the west and east injections that comprise a single substorm event. The only parameter that must vary from one substorm to the next is $t$, the number of seconds since onset. The results for each injection are summed together to produce a total value of $N$ for each electron energy. We also include electrons that have made more than one complete orbit around the planet (known as drift echoes) by adding integer multiples of 360° to $\phi$.

### 3.8. Energetic Electron Precipitation

In the current model, the precipitation flux $P$ is assumed to be equal to the electron loss rate. In units of degrees$^{-1}$ (azimuth), $R_E^{-1}$ (radius), s$^{-1}$, eV$^{-1}$,

$$P = \frac{N}{\tau} \quad (\text{deg}^{-1}\ R_E^{-1}\ \text{s}^{-1}\ \text{eV}^{-1}) \tag{11}$$

where $N$ is the magnetospheric density of electrons, given by equation (10), summed over all injections occurring in the preceding 12 h; $\tau$ is a fifth of the strong diffusion limit (equation (6)) is $\tau$. In the dipole field approximation, an infinitesimally narrow flux tube with radial size d$R$ ($R_E$) in the equatorial plane, and azimuthal size d$\phi$ (degrees), will have an ionospheric footprint of area

$$\frac{\pi}{180}\frac{(6.45\times10^6)^2}{\sqrt{L^4-L^3}}\,\text{d}R\,\text{d}\phi \quad (\text{m}^2) \tag{12}$$

With this conversion factor, the precipitation flux can be written in more convenient units as

$$P = \frac{N}{\tau}\frac{180}{\pi}\frac{\sqrt{L^4-L^3}}{(6.45\times10^6)^2} \quad (\text{m}^{-2}\ \text{s}^{-1}\ \text{eV}^{-1}) \tag{13}$$

### 3.9. Ionospheric Electron Density

The ionospheric electron density is calculated with the steady state equation

$$N_e = \sqrt{\frac{Q+Q_{\text{quiet}}}{\alpha_{\text{eff}}}} \tag{14}$$

where $Q_{\text{quiet}}$ is the quiet production rate and $\alpha_{\text{eff}}$ is the effective recombination rate. The quiet production rates are taken from *Barabash et al.* [2012], which are given for various solar zenith angles. The effective recombination rates are calculated using the Sodankylä Ion Chemistry model [*Turunen et al.*, 1996]. $Q$ is the production rate due to the precipitating electrons. It is calculated using the modeled precipitation rates, $P$, over the range of energies from 20 keV to 300 keV, following the method of *Semeter and Kamalabadi* [2005], who provide tabulated energy dissipation functions based on laboratory measurements.

## 4. Results

The model electron density profiles can be used to predict the response of ground-based instruments including riometers and VLF radio receivers. Ionospheric absorption is calculated using the Appleton-Hartree equation [see, e.g., *Davies*, 1966], with neutral densities from the US Naval Research Laboratory Mass Spectrometer and Incoherent Scatter Radar, ground through Exosphere, revised in the year 2000 (NRLMSISE-00) neutral atmosphere model [*Picone et al.*, 2002], and effective momentum-transfer collision frequencies from *Beharrell and Honary* [2008, and references therein]. Figure 3 shows the resulting model cosmic noise absorption following a single typical substorm, using the parameters specified in section 3.7. The contours represent the levels of absorption at 38.2 MHz and are evenly spaced at multiples of 0.3 dB. Each of the six plots shows the absorption at a different elapsed time since the substorm onset. Although the plots only cover the first 90 min of a substorm, trapped electrons that are drifting for up to 12 h are included in our model runs. The results in Figure 3 are similar to the absorption maps produced from a survey of substorm riometer observations by *Berkey et al.* [1974], showing the westward traveling surge, the eastward drift of absorption patches, and small levels of absorption lingering hours after the substorm onset. At geosynchronous orbit ($L = 6.6\ R_E$) trapped 200 keV electrons with pitch angles used in the model ($\alpha_0 = 39.5°$) have drift periods of around 35 min, whereas 30 keV electrons that are otherwise identical orbit the planet in around 215 min. This dispersion is the cause of the azimuthally near-uniform absorption pattern 90 min after onset, shown in Figure 3f.

### 4.1. Comparison With IRIS Data

Figure 4a shows the model electron precipitation (20 keV–300 keV) calculated for the location of the IRIS riometer in Kilpisjärvi, Finland (69.05°N, 20.79°E, L shell = 6.1), during 5 days in April/May 2007. The timing of all 61 substorm onsets detected by SuperMAG during this period are represented by vertical blue lines. The model precipitation comprises the individual precipitation from each of the magnetometer-detected substorms added together. In Figure 4b is the corresponding model cosmic noise absorption, together with measurements from IRIS (wide beam, with corrections for the oblique angles of the beam's edge). In this model run, the substorms are treated as identical, typical substorms, each injecting $N_T = 10^{28}$ electrons with energies of 20 keV to 300 keV. The elapsed number of seconds since substorm onset, $t$, is the only

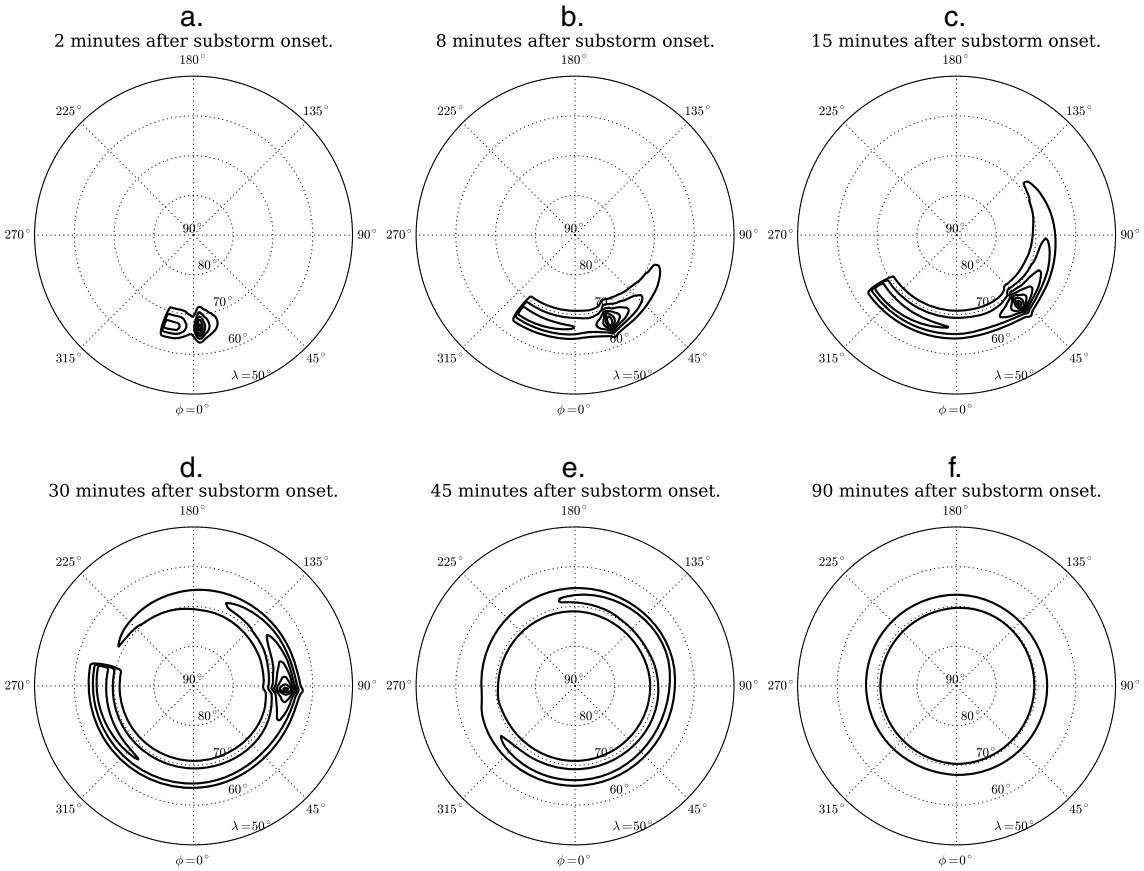


**Figure 3.** Ionospheric absorption at various elapsed times since the onset of a typical substorm, as a function of magnetic latitude ($\lambda$), and magnetic azimuth angle ($\phi$). Magnetic midnight is at $\phi = 0°$. The absorption is calculated for 38.2 MHz radio waves, with contours evenly spaced at multiples of 0.3 dB.

model parameter that varies between each substorm. It is determined by the onset times in the SuperMAG substorm database.

This period was chosen because it contains a good number of substorms with varied spacing and good data availability from the IRIS riometer, the nearby subionospheric VLF receiver at the Sodankylä Geophysical Observatory (SGO), and the SuperMAG substorm database. It was also close to solar minimum, a time when most other contributors to absorption, such as solar proton events and direct ionization by X-rays emitted by large solar flares, are far fewer in number. During the 5 day period there was only minor flare activity,

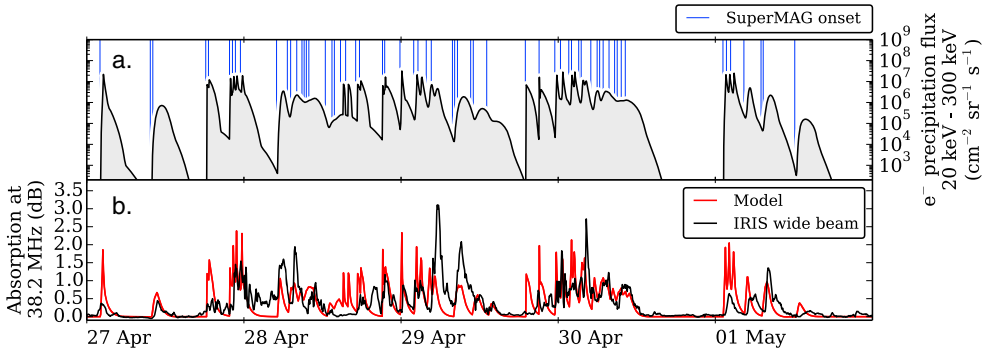


**Figure 4.** Comparison of IRIS riometer data with the model, for a 5 day period in 2007. Model parameters are those of a typical substorm injection for each of the 61 SuperMAG-detected substorms. (a) Model energetic electron precipitation at IRIS, integrated in energy. Blue lines indicate substorm onset times. (b) Comparison of IRIS wide-beam riometer absorption with the corresponding model absorption.

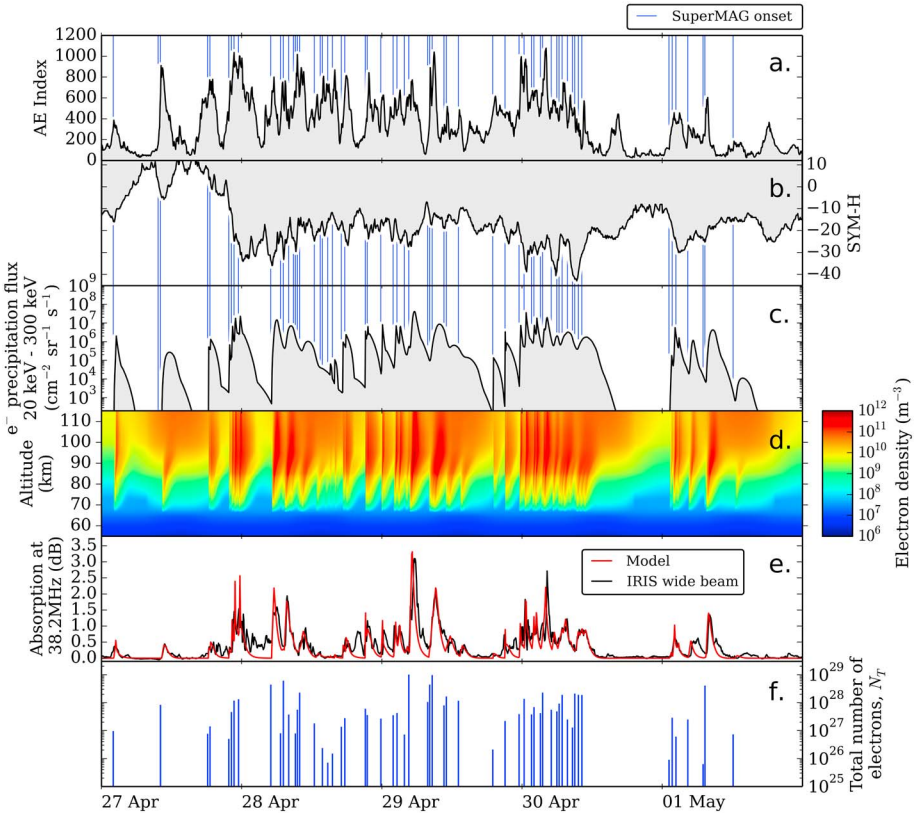


**Figure 5.** Comparison of IRIS riometer data with the model, for a 5 day period in 2007. Model parameters are those of a typical substorm injection, except for the total number of electrons injected during each substorm, $N_T$, which is allowed to vary from one substorm to the next. The values of $N_T$ are fitted so that the model best fits the IRIS data. The vertical blue lines indicate the SuperMAG-detected onset time of each substorm, and those in the panel f show the fitted values of $N_T$ for each substorm.

peaking with a B7 flare. The X-rays emitted by flares of this magnitude cause negligible ionospheric absorption. A high-speed solar wind stream began on 27 April at around 16 UT, and peaked on 29 April with a speed of 717 km $s^{-1}$. The geoeffectiveness of the high-speed stream is apparent in the *AE* index and *SYM-H*, shown in Figure 5. The large upswings in *AE* index are directly related to substorm activity, while the observed *SYM-H* values between around −10 and −40 are indicative of a mild geomagnetic storm.

In Figure 5, the model is rerun with the total number of electrons injected in each substorm, $N_T$, allowed to vary. The values of $N_T$ are those that give the best least squares fit between the data and the model. They are found with an iterative Markov chain method, by adjusting the value of $N_T$ for each injection in turn, and calculating the square difference between the model and the data.

During times of enhanced *AE* index the model energy-integrated electron precipitation flux also shows enhancements (Figure 5c). However, on the afternoons of 30 April and 1 May there are increases in *AE* index that are not represented in the model precipitation flux. This is unavoidable given that there are no SuperMAG-detected substorm onsets during these times.

Following the method outlined in section 3.9, energy-dependent precipitation values are used to calculate the ionospheric electron density profiles (Figure 5d), which are in turn used to calculate cosmic noise absorption (Figure 5e). The close correspondence between the model results and data shows that the majority of absorption events during this period are well represented by the model of substorm-induced electron precipitation.

Figure 5f shows the total number of electrons injected in each substorm, $N_T$, inferred by fitting the model absorption to the data. The mean of the fitted $N_T$ values is $1.15 \times 10^{28}$ and the maximum is $9.6 \times 10^{28}$ electrons.

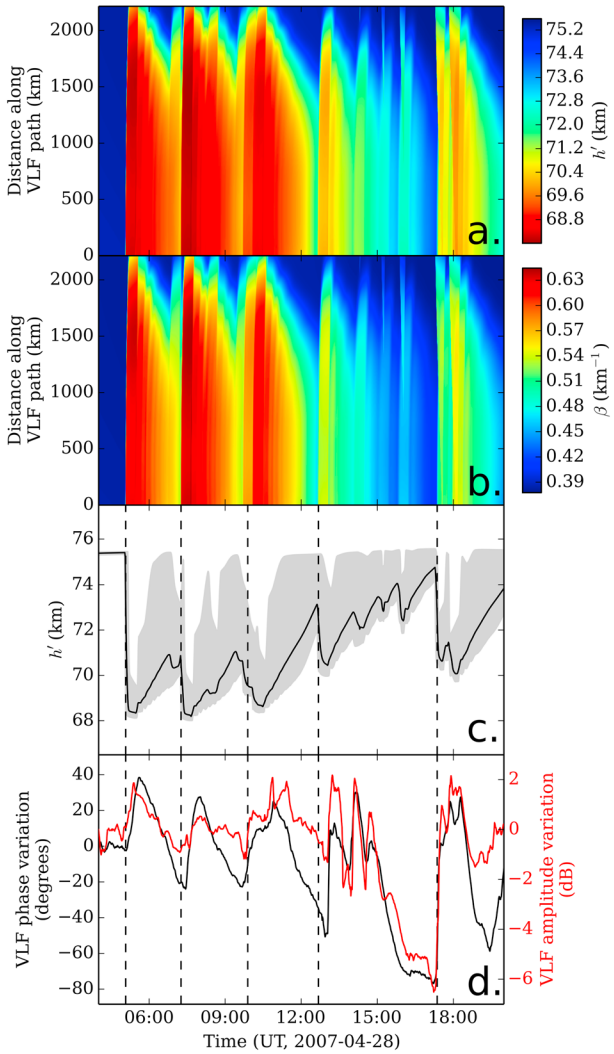


**Figure 6.** The modeled ionosphere along the path of the NRK to SGO subionospheric VLF signal. (a) The height of the ionosphere along the path (the *y* axis is the distance from the transmitter to the VLF receiver along the great circle path). (b) The steepness of the ionosphere along the VLF signal path. (c) The mean model ionospheric height along the path (solid line) and the range of heights along the path (shaded region). The dashed vertical lines indicate the 5 times when the mean ionospheric height along the path changes most rapidly. (d) The measured VLF amplitude (red) and phase (black) at the SGO receiver.

It is interesting to note that the first two substorms on 27 April produced similar levels of absorption at the IRIS riometer, but both the *AE* index and the inferred value of $N_T$ were larger in the second of the two substorms. This is because *AE* and $N_T$ are (ideally) independent of the planet's rotation, but the local time of the riometer during each event meant that it was farther from the near-midnight injection during the second substorm. As a result a smaller proportion of the injected electrons reached its location.

### 4.2. Comparison With Subionospheric VLF Data

The propagation of a subionospheric low-frequency radio wave depends on the properties of the waveguide formed between the ground and ionosphere. Variations in the electron number density profile at the bottomside of the ionosphere determine the phase and amplitude of the signal that arrives at a remote receiver, having traveled subionospherically from the transmitter. One approach for representing the electron density profile is to use the parameters $h'$ and $\beta$ from the Wait ionosphere [*Wait and Spies*, 1964]. Here $h'$ is the reference height, and $\beta$ describes the steepness of the profile at $h'$. A reduction in the height of the ionosphere will cause a positive phase advancement, but the amplitude variation is the result of a more complex relationship depending on the summation of the waveguide modes and may be positive or negative.

Figure 6 shows results for the 37.5 kHz radio wave propagating between the NRK transmitter in Grindavik, Iceland, and the SGO subionospheric VLF receiver in Sodankylä, Finland. This path is part of the AARDDVARK network [*Clilverd et al.*, 2009]. The results cover a single day from the same period in 2007 used in the comparison with IRIS riometer absorption in the previous section. In Figures 6a and 6b, the parameters $h'$ and $\beta$ are calculated along the great circle path between NRK and SGO by fitting the Wait ionosphere to the substorm model results. A distance of 0 km on the *y* axis corresponds to the position of the transmitter. The mean ionospheric height along the path is given by the solid black line in Figures 6c, where the shaded area represents the range of ionospheric heights along the path. A good correlation exists between the model ionospheric height and the phase and amplitude measured by the SGO receiver. The vertical dashed lines indicate the times of maximum change in the model ionospheric height, $h'$. As expected [e.g., *Clilverd et al.*, 2008, 2009], a reduction in ionospheric height due to precipitating electrons leads to an advancement of the received phase.

In Figure 6 the model uses the values of $N_T$, the number of energetic electrons in each substorm injection, found in the previous section by fitting the model to IRIS absorption data. These values provide a considerable improvement to the correlation between ionospheric height and the measured VLF phase, compared

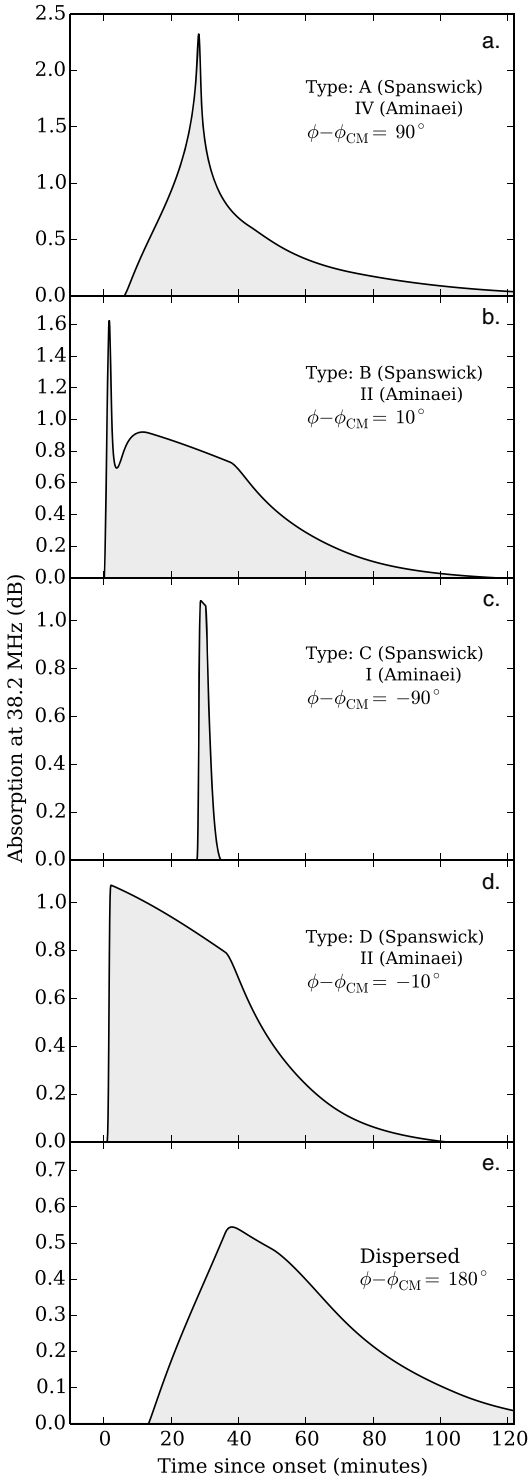


**Figure 7.** Spike events observed in the model absorption. (a) Type A, a spike embedded in drifting electrons; (b) type B, a spike preceding drifting electrons; (c) type C, a solitary spike; (d) type D, a spike with sharp rise time and slow fall time. (e) The model absorption on the dayside from the precipitation of dispersed drifting electrons.

to using the same $N_T$ for each substorm injection (not shown). The Pearson correlation between the mean ionospheric height and VLF phase improves from a value of −0.14 (low correlation) when using fixed values of $N_T$, to −0.56 (moderate negative correlation) with the fitted values of $N_T$.

This result confirms the usefulness of the substorm precipitation model in providing context for VLF phase and amplitude observations. The modeled injection of energetic electrons in a region close to magnetic midnight, as described in section 3, with timing based on the SuperMAG substorm database, and magnitudes determined from a single riometer site is able to successfully predict the VLF perturbation timings on the Iceland to Finland path. The relative perturbations in $h'$, from substorm to substorm, predicted by the model are consistent with the levels of phase perturbations observed. This is expected if the change in ionization along the VLF path is reasonably represented in the substorm model at energies of >100 keV.

### 4.3. Riometer Spike Events

Four distinct types of spike events are categorized by *Spanswick et al.* [2005], these are as follows: (A) a spike embedded in slowly varying, diffuse, precipitation; (B) a spike preceding diffuse precipitation; (C) a solitary spike; and (D) spike events with a sharp rise time (<3 min) and slow decay time (>15 min). The sharp rise of less than 3 min is a strong indicator of dispersionless injection and distinguishes these events from dispersed electrons [*Spanswick et al.*, 2007].

Figure 7 show all four of the spike categories occurring in the current model, each at a different azimuthal location, $\phi$ (i.e., magnetic local time) relative to the central meridian, $\phi_{CM}$. The azimuthal angles, in degrees, are equivalent to MLT, and may be converted to MLT (hours) by dividing by 15. The parameters used to generate Figure 7 are those of a typical substorm, defined in section 3.7. The model is able to represent all of the recognized variations of spike events because, in line with *Kennel* [1995], the energetic electron injections are concentrated at the dipolarization fronts, at the edges of the substorm current wedge, instead of being uniformly distributed across magnetic midnight in a single large injection region.

The model spike that resembles a category D event (Figure 7d) has a rise time of ~1 min, inside the 3 min limit specified by *Spanswick et al.* [2007], this differentiates it from the dispersed events that occur farther from the injection region (Figure 7e).

*Aminaei et al.* [2006] independently categorized spike events, with four types denoted by Roman numerals, and presented the observed local time distributions of each. Their type I is a solitary spike, equivalent to type C; type II contains both types B and D events; and type IV shares the definition of type A. Type III spikes events are those in which a spike appears after more diffuse absorption. They are a rarely observed class, representing only 1 in 18 observed spikes. This scarcity could indicate that type III spikes are not a true independent category but are instead a coincidental occurrence of a solitary spike with an unrelated earlier injection.

The distribution of type IV (A) events is skewed toward eastward magnetic local times, whereas type II (B and D) events are mostly observed around central locations (~22:45 MLT), these results match our model predictions. The most common local time for type I (C) events is the most westward of the three categories, as predicted by the model, but there are a substantial number of these events to the east. It is not clear if the eastward type I (C) events are misclassified type IV (A) events, as could happen if the level of diffuse absorption is low, or if the fault is with the assumptions made in our model. There is a large amount of spread in each of the local time distributions reported by *Aminaei et al.* [2006], leading to considerable overlapping. This could be due to the different locations of each substorm's central meridian.

## 5. Discussion

The substorm model is capable of representing medium-energy electron precipitation well, only requiring the number of electrons injected in each substorm to be adjusted for an overall good fit between the model and IRIS riometer data (see Figure 5). This does not mean that the magnitude of each substorm is the only variable that is important; changes in the spectra of injected electrons can have similar effects. Without more information, it would be difficult to untangle the effects of the magnitude, and spectra of injections to fit them simultaneously. This information could come from, for example, satellite measurements of the injection spectra. This is beyond the scope of the current study, but it is something we are currently working toward.

During the 5 day period in April/May 2007 for which the model was run, a high-speed solar wind stream hit the Earth, causing a moderate geomagnetic storm. This resulted in an increase in the frequency of substorms, and significant populations of electrons injected by different substorms existed simultaneously in the magnetosphere. With a simple linear addition of the injected electron populations, the model appears to cope well with the concurrent substorms.

The model relies on reliable detection of substorm onsets, without them the model will not show any precipitation. At around 20 UT on 28 April, the IRIS riometer measured an enhancement in absorption (Figure 5e) that was not accompanied by an onset detection in the SuperMAG substorm database. Two properties of the event suggest that this was not a substorm: there was no corresponding enhancement in the *AE* index, and the rise time of the absorption enhancement was longer than the decay time. One possibility is that it is a result of the increase in dynamic solar wind pressure (not shown), which grew from 1.8 nPa at 18 UT, to 2.8 nPa at 20 UT, distorting the magnetosphere and causing electrons to enter the loss cone.

A simplifying assumption made in the model is that pitch angle diffusion rates are constant. In other words, at a particular location and time the proportion of electrons precipitating into the ionosphere is proportional to the trapped flux at that location. In reality the diffusion rate has a nonlinear relationship with the trapped electron flux, in part because chorus waves are strongly enhanced by substorms [*Meredith et al.*, 2001]. As a result intense chorus waves coincide with the injected drifting electrons in the morning sector, leading to higher pitch angle diffusion rates than in the afternoon. In the future we hope to extend the model to take into account the varying levels of pitch angle diffusion in each sector and include a more nuanced energy dependence.

In times of prolonged substorm activity (lasting approximately days), such as during geomagnetic storms and high-speed solar wind streams, a small proportion of the injected medium-energy electrons can be accelerated by the chorus waves to MeV energies [*Summers et al.*, 2007; *Ni et al.*, 2011]. *Reeves et al.* [2003] examined 276 geomagnetic storms over a whole solar cycle, finding that around half of the storms increased fluxes of relativistic electrons (1 to 3 MeV) in the outer radiation belt, one fifth of storms decreased fluxes,

and the remaining storms made negligible difference to the relativistic fluxes. The probability that a storm will increase or decrease the population of relativistic electrons was found to be essentially the same throughout the outer radiation belt, from $L = 4$ to geosynchronous orbit. The variability in the response of relativistic fluxes to storm activity is a result of the competing effects of the acceleration and loss processes [*Summers et al.*, 2007]. The relatively low flux of MeV electrons compared to medium-energy electrons, even during storms [see, e.g., *Gabrielse et al.*, 2012], combined with the insensitivity of riometers to relativistic electron precipitation, allows us to neglect relativistic electrons when modeling ionospheric cosmic noise absorption. In contrast, subionospheric VLF propagation is most sensitive to ionization caused by relativistic electron precipitation (>100 keV) [*Clilverd et al.*, 2008]. Therefore, accurate modeling of VLF propagation is likely to benefit from the inclusion of MeV electrons.

The various types of spike events observed in the result emerge naturally from equation (10). They are a result of azimuthal asymmetries in the model. The primary asymmetry being that electrons only drift eastward, so dispersed particle precipitation is only observed to the east of the injection (except for drift echoes). Expanding an earlier one-dimensional (radial only) model of substorm injection to include the azimuthal drift of electrons, *Liang et al.* [2007] were able to reproduce spikes of type C (solitary) and D (fast rise, slow decay), as well as dispersed signatures of precipitation (slow rise and slow decay). Sharp spikes were found at the western edge of the injection region, and spikes with slow decay were found at the eastern edge. However, between the two edges of their uniform injection region a range of spikes exist with intermediate decay times. The ability of the current model to represent spike events more accurately than previous models can be attributed to the assumptions that energetic electron injections are concentrated in the regions undergoing dipolarization and that these regions expand from a central meridian. Such features have been recognized for some time [e.g., *Nagai*, 1982; *Lopez et al.*, 1989] but are often neglected in other models. For example, while the injection region of *Liang et al.* [2007] expands over time, it is a single, azimuthally uniform region.

## 6. Conclusion

We have constructed a model of substorm injection that, when combined with onset timing provided by the SuperMAG substorm database, is capable of reproducing ground-based observations of medium-energy electron precipitation at energies from 20 keV to 300 keV. During a period in April/May 2007, 61 substorm injections are modeled, and the number of energetic electrons injected during each substorm is estimated. The mean is found to be $1.15 \times 10^{28}$, in agreement with previous estimates by *Atkinson* [1972, 1984].

The four distinct categories of riometer spike events, as well as dispersed precipitation signatures, emerge in the model results. The results indicate that each type of spike event are observations of the same phenomena, made at different locations relative to the central meridian. These locations appear to be consistent with the statistical observations of *Aminaei et al.* [2006], although there is some uncertainty due to the variation of the central meridian location from one substorm to the next.

To investigate the contribution of substorm precipitation to changes in climate, the model may be used as an input to atmospheric chemistry and climate models, such as the Sodankylä Ion Chemistry model [*Turunen et al.*, 1996] or the Whole Atmosphere Community Climate Model (WACCM) [see, e.g., *Garcia et al.*, 2007]. In this case, onset timing could be taken from, for example, the Minimal Substorm Model [*Freeman and Morley*, 2004] for a range of possible future solar wind parameters.

It is well known that energetic particle precipitation causes significant changes in atmospheric chemistry, not just at ionospheric altitudes, but as low as the stratosphere, where up to 40% of the $NO_x$ in the polar region can be attributed to the descent of $NO_x$ produced at high altitudes by particle precipitation. Results from WACCM underestimate this contribution to stratospheric $NO_x$ by around a factor of 2 [*Fang et al.*, 2008]. Currently, the medium-energy electron precipitation used in the WACCM model are averaged patterns from *Codrescu et al.* [1997]. These are based on the Medium Energy Proton and Electron Detector (MEPED) instruments onboard the NOAA/POES satellites data, with a different pattern for each of several levels of geomagnetic activity. Averaging of the data in this way is likely to smooth over the small-scale (temporal and spatial) variations in precipitation following a substorm injection. Incorporating the electron precipitation values from the substorm model could improve the accuracy of the WACCM NOx simulations.

**Acknowledgments**

We thank Annika Seppälä for running the Sodankylä Ion Chemistry model to provide us with ionospheric effective recombination rates. Data from the IRIS riometer (PI Farideh Honary) is available from Lancaster University (http://spears.lancs.ac.uk/data/). Subionospheric VLF data from the AARDDVARK Network can be obtained by contacting Mark A. Clilverd or Craig J. Rodger. The NRLMSISE-00 neutral atmosphere model code can be obtained from the Community Coordinated Modeling Center (http://ccmc.gsfc.nasa.gov/modelweb/atmos/nrlmsise00.html). Substorm onset timing data, based on ground-based magnetometer data and provided by SuperMAG, are available from the John Hopkins Applied Physics Laboratory (http://supermag.jhuapl.edu/substorms/). For the SuperMAG data we gratefully acknowledge the following: Intermagnet; USGS, Jeffrey J. Love; Danish Meteorological Institute; CARISMA, Ian Mann; CANMOS; The S-RAMP Database, K. Yumoto and K. Shiokawa; The SPIDR database; AARI, Oleg Troshichev; The MACCS program, M. Engebretson, Geomagnetism Unit of the Geological Survey of Canada; GIMA; MEASURE, UCLA IGPP and Florida Institute of Technology; SAMBA, Eftyhia Zesta; 210 Chain, K. Yumoto; SAMNET, Farideh Honary; The institutes who maintain the IMAGE magnetometer array, Eija Tanskanen; PENGUIN; AUTUMN, Martin Conners; Greenland magnetometers operated by DTU Space; South Pole and McMurdo Magnetometer, Louis J. Lanzarotti and Alan T. Weatherwax ; ICESTAR; RAPIDMAG; PENGUIn; British Artarctic Survey; McMac, Peter Chi; BGS, Susan Macmillan; Pushkov Institute of Terrestrial Magnetism, Ionosphere and Radio Wave Propagation (IZMIRAN); and SuperMAG, Jesper W. Gjerloev. This work was supported by the Natural Environmental Research Council grant NE/J008125/1.

Larry Kepko thanks the reviewers for their assistance in evaluating this paper.

## References

Akasofu, S-I. (1964), The development of the auroral substorm, *Planet. Space Sci.*, *12*, 273–282.

Aminaei, A., F. Honary, A. J. Kavanagh, E. Spanswick, and A. Viljanen (2006), Characteristics of night-time absorption spike events, *Ann. Geophys.*, *24*, 1887–1904.

Angelopoulos, V. (2008), The THEMIS mission, *Space Sci. Rev.*, *141*, 5–34.

Arnoldy, R. L., and T. E. Moore (1983), Longitudinal structure of substorm injections at synchronous orbit, *J. Geophys. Res.*, *88*, 6213–6220.

Atkinson, G. (1972), Magnetospheric flows and substorms, in *Magnetosphere–Ionosphere Interactions, Proceedings of the Advanced Study Institute at Dalseter, Norway, 14–23 April 1971*, edited by K. Folkestad, pp. 203–216, Scandinavian Univ. Books, Oslo.

Atkinson, G. (1984), The role of currents in plasma redistribution, in *Magnetospheric Currents*, edited by T. A. Potemra, pp. 325–330, Washington, D. C., doi:10.1029/GM028p0325.

Baker, D. N., R. D. Belian, P. R. Higbie, and E. W. Hones (1979), High-energy magnetospheric protons and their dependence on geomagnetic and interplanetary conditions, *J. Geophys. Res.*, *84*, 7138–7154.

Baker, D. N., J. B. Blake, L. B. Callis, R. D. Belian, and T. E. Cayton (1989), Relativistic electrons near geostationary orbit: Evidence for internal magnetospheric acceleration, *Geophys. Res. Lett.*, *16*(6), 559–562.

Barabash, V., A. Osepian, P. Dalin, and S. Kirkwood (2012), Electron density profiles in the quiet lower ionosphere based on the results of modeling and experimental data, *Ann. Geophys.*, *30*, 1345–1360, doi:10.5194/angeo-30-1345-2012.

Baumjohann, W., and R. A. Treumann (1996), *Basic Space Plasma Physics*, Imperial College Press, London.

Beharrell, M., and F. Honary (2008), A new method for deducing the effective collision frequency profile in the D-region, *J. Geophys. Res.*, *113*, A05303, doi:10.1029/2007JA012650.

Berkey, F. T., V. M. Driatskiy, K. Henriksen, B. Hultqvist, D. H. Jelly, T. I. Shchuka, A. Theander, and J. Ylindemi (1974), A synoptic investigation of particle precipitation dynamics for 60 substorms in IQSY (1964–1965) and IASY (1969), *Planet. Space Sci.*, *22*(2), 255–307, doi:10.1016/0032-0633(74)90028-2.

Birn, J. (2011), Magnetotail dynamics: Survey of recent progress, in *The Dynamic Magnetosphere, IAGA Spec. Sopron Book Ser. 3*, edited by W. Liu and M. Fujimoto, pp. 49–63, Springer, Netherlands, doi:10.1007/978-94-007-0501-2_4.

Christon, S. P., D. J. Williams, D. G. Mitchell, C. Y. Huang, and L. A. Frank (1991), Spectral characteristics of plasma sheet ion and electron populations during disturbed geomagnetic conditions, *J. Geophys. Res.*, *96*, 1–22, doi:10.1029/90JA01633.

Clilverd, M. A., et al. (2008), Energetic electron precipitation during substorm injection events: High-latitude fluxes and an unexpected midlatitude signature, *J. Geophys. Res.*, *113*, A10311, doi:10.1029/2008JA013220.

Clilverd, M. A., et al. (2009), Remote sensing space weather events: Antarctic-Arctic Radiation-belt (Dynamic) Deposition-VLF Atmospheric Research Konsortium network, *Space Weather*, *7*, S04001, doi:10.1029/2008SW000412.

Codrescu, M. V., T. J. Fuller-Rowell, R. G. Roble, and D. S. Evans (1997), Medium energy particle precipitation influences on the mesosphere and lower thermosphere, J. Geophys. Res., *102*, *A9*, 19, 977–19, 988, doi:10.1029/97JA01728.

Cresswell-Moorcock, K., C. J. Rodger, A. Kero, A. B. Collier, M. A. Clilverd, I. Häggström, and T. Pitkänen (2013), A reexamination of latitudinal limits of substorm-produced energetic electron precipitation, *J. Geophys. Res. Space Physics*, *118*, 6694–6705, doi:10.1002/jgra.50598.

Davies, K. (1966), *Ionospheric Radio Propagation*, Dover Publ., New York.

Fang, X., C. E. Randall, D. Lummerzheim, S. C. Solomon, M. J. Mills, C. H. Jackman, D. R. Marsh, W. Wang, and G. Lu (2008), On the effect of medium energy electron precipitation on the Earth's middle and low atmosphere, Abstract SA33A-1630 presented at 2008 Fall Meeting AGU, San Francisco, Calif.

Freeman, M. P., and S. K. Morley (2004), A minimal substorm model that explains the observed statistical distribution of times between substorms, *Geophys. Res. Lett.*, *31*, L12807, doi:10.1029/2004GL019989.

Gabrielse, C., V. Angelopoulos, A. Runov, and D. L. Turner (2012), The effects of transient, localized electric fields on equatorial electron acceleration and transport toward the inner magnetosphere, *J. Geophys. Res.*, *117*, A10213, doi:10.1029/2012JA017873.

Garcia, R. R., D. R. Marsh, D. E. Kinnison, B. A. Boville, and F. Sassi (2007), Simulation of secular trends in the middle atmosphere, 1950–2003, *J. Geophys. Res.*, *112*, D09301, doi:10.1029/2006JD007485.

Hargreaves, J. K. (2007), Auroral radio absorption: The prediction question, *Adv. Space Res.*, *45*, 1075–1092.

Kabin, K., E. Spanswick, R. Rankin, E. Donovan, and J. C. Samson (2011), Modeling the relationship between substorm dipolarization and dispersionless injection, *J. Geophys. Res.*, *116*, A04201, doi:10.1029/2010JA015736.

Kennel, C. F. (1969), Consequences of a magnetospheric plasma, *Rev. Geophys.*, *7*, 379–419.

Kennel, C. F. (1995), *Convection and Substorms: Paradigms of Magnetospheric Phenomenology, Int. Ser. on Astron. Astrophys.*, Oxford Univ. Press, New York.

Kennel, C. F., and H. E. Petschek (1966), Limit on stably trapped particle fluxes, *J. Geophys. Res.*, *71*, 1–28.

Kim, H.-J., A. A. Chan, R. A. Wolf, and J. Birn (2000), Can substorms produce relativistic outer belt electrons?, *J. Geophys. Res.*, *105*(A4), 7721–7735, doi:10.1029/1999JA900465.

Kokobun, S., and R. L. McPherron (1981), Substorm signatures at synchronous altitude, *J. Geophys. Res.*, *86*, 11,265–11,277, doi:10.1029/JA086iA13p11265.

Lazutin, L. L., T. V. Kozelova, N. P. Meredith, M. Danielides, B. V. Kozelov, J. Jussila, and A. Korth (2007), Studies of substorm on March 12, 1991: 2. Auroral electrons. Acceleration, injection, and dynamics, *Cosmic Res.*, *45*(2), 89–96, doi:10.1134/S0010952507020013.

Li, W., R. M. Thorne, V. Angelopoulos, J. Bortnik, C. M. Cully, B. Ni, O. LeContel, A. Roux, U. Auster, and W. Magnes (2009), Global distribution of whistler-mode chorus waves observed on the THEMIS spacecraft, *Geophys. Res. Lett.*, *36*, L09104, doi:10.1029/2009GL037595.

Li, X., D. N. Baker, M. Temerin, G. D. Reeves, and R. D. Belian (1998), Simulation of dispersionless injections and drift echoes of energetic electrons associated with substorms, *Geophys. Res. Lett.*, *25*(20), 3763–3766.

Liang, J., W. W. Liu, E. Spanswick, and E. F. Donovan (2007), Azimuthal structures of substorm electron injection and their signatures in riometer observations, *J. Geophys. Res.*, *112*, A09209, doi:10.1029/2007JA012354.

Liu, W. W., J. Liang, E. Spanswick, and E. F. Donovan (2007), Remote-sensing magnetospheric dynamics with riometers: Observation and theory, *J. Geophys. Res.*, *112*, A05214, doi:10.1029/2006JA012115.

Lopez, R. E., A. T. Y. Lui, D. G. Sibeck, K. Takahashi, and R. W. McEntire (1989), On the relationship between the energetic particle flux morphology and the change in the magnetic field magnitude during substorms, *J. Geophys. Res.*, *94*, 17,105–17,119, doi:10.1029/JA094iA12p17105.

Lui, A. T. Y. (2007), Physical processes for magnetospheric substorm expansion onsets, in *The Dynamic Magnetosphere, IAGA Spec. Sopron Book Ser. 3*, edited by W. Liu and M. Fujimoto, pp. 65–115, Springer, Netherlands, doi:10.1007/978-94-007-0501-2_5.

Lyon, J. G., R. E. Lopez, C. C. Goodrich, M. Wiltberger, and K. Papadopoulus (1998), Simulation of the March 9, 1995, substorm: Auroral brightening and the onset of lobe reconnection, *Geophys. Res. Lett.*, *25*(15), 3039–3042.

Meredith, N. P., R. B. Horne, and R. R. Anderson (2001), Substorm dependence of chorus amplitudes: Implications for the acceleration of electrons to relativistic energies, *J. Geophys. Res.*, *106*(A7), 13,165–13,178, doi:10.1029/2000JA900156.

Nagai, T. (1982), Observed magnetic substorm signatures at synchronous altitude, *J. Geophys. Res.*, *87*, 4405–4417, doi:10.1029/JA087iA06p04405.

Nagai, T. (1991), An empirical model of substorm-related magnetic field variations at synchronous orbit, in *Magnetospheric Substorms, Geophys. Monogr. Ser.*, vol. 64, edited by J. R. Kan et al., pp. 91–95, AGU, Washington, D. C.

Newell, P. T., and J. W. Gjerloev (2011), Evaluation of SuperMAG auroral electrojet indices as indicators of substorms and auroral power, *J. Geophys. Res.*, *116*, A12211, doi:10.1029/2011JA016779.

Ni, B., R. M. Thorne, N. P. Meredith, R. B. Horne, and Y. Y. Shprits (2011), Resonant scattering of plasma sheet electrons leading to diffuse auroral precipitation: 2. Evaluation for whistler mode chorus waves, *J. Geophys. Res.*, *116*, A04219, doi:10.1029/2010JA016233.

Northrop, T. G. (1966), Adiabatic theory of charged particle motion, in *Radiation Trapped in The Earth's Magnetic Field, Proceedings of the Advanced Study Institute Held at the Chr. Michelsen Institute, Bergen, Norway August 16–September 3, 1965*, edited by B. M. McCormac, pp. 26–44, D. Reidel, Dordrecht, Netherlands.

Ohtani, S., K. Takahashi, L. J. Zanetti, T. A. Potemra, R. W. McEntire, and T. Iijima (1991), Tail current disruption in the geosynchronous region, in *Magnetospheric Substorms, Geophys. Monogr. Ser.*, vol. 64, edited by J. R. Kan et al., p. 131, AGU, Washington D. C.

Parthasarathy, R., and F. T. Berkey (1965), Auroral zone studies of sudden onset radio wave absorption events using multiple-station and multiple-frequency data, *J. Geophys. Res.*, *70*(89), 415–421.

Picone, J. M., A. E. Hedin, D. P. Drob, and A. C. Aikin (2002), NRLMSISE-00 empirical model of the atmosphere: Statistical comparisons and scientific issues, *J. Geophys. Res.*, *107*(A12), 1468, doi:10.1029/2002JA009430.

Raeder, J., D. Larson, W. Li, E. L. Kepko, and T. Fuller-Rowell (2008), OpenGGCM simulations for the THEMIS mission, *Space Sci. Rev.*, *141*, 535–555.

Reeves, G. D. (1998), New perspectives on substorm injections, in *Proceedings of the Fourth International Conference on Substorms, ICS-4, Hamanako, Japan, March, 1998*, edited by S. Kokubun and Y. Kamide, p. 785, Kluwer Acad., Dordrecht, Netherlands.

Reeves, G. D., K. L. McAdams, R. H. W. Friedel, and T. P. O'Brien (2003), Acceleration and loss of relativistic electrons during geomagnetic storms, *Geophys. Res. Lett.*, *30*(10), 1529, doi:10.1029/2002GL016513.

Robert, P., R. Gendrin, S. Perraut, A. Roux, and A. Pedersen (1984), GEOS 2 identification of rapidly moving current structures in the equatorial outer magnetosphere during substorms, *J. Geophys. Res.*, *89*, 819–840, doi:10.1029/JA089iA02p00819.

Rodger, C. J., M. A. Clilverd, A. J. Kavanagh, C. E. J. CWatt, P. T. Verronen, and T. Raita (2012), Contrasting the responses of three different ground-based instruments to energetic electron precipitation, *Radio Sci.*, *47*(2), RS2021, doi:10.1029/2011RS004971.

Sarafopoulus, D. V. (2008), A physical mechanism producing suprathermal populations and initiating substorms in the Earth's magnetotail, *Ann. Geophys.*, *26*, 1617–1639.

Sarris, T. E., X. Li, N. Tsaggas, and N. Paschalidis (2002), Modeling energetic particle injections in dynamic pulse fields with varying propagation speeds, *J. Geophys. Res.*, *107*(A3), 1033, doi:10.1029/2001JA900166.

Semeter, J., and F. Kamalabadi (2005), Determination of primary electron spectra from incoherent scatter radar measurements of the auroral E region, *Radio Sci.*, *40*, RS2006, doi:10.1029/2004RS003042.

Spanswick, E., E. Donovan, W. Liu, D. Wallis, A. Aasnes, T. Hiebert, B. Jackel, M. Henderson, and H. Frey (2005), Substorm associated spikes in high energy particle precipitation, in *The Inner Magnetosphere: Physics and Modeling, Geophys. Monogr. Ser.*, vol. 155, edited by T. I. Pulkkinen, N. A. Tsyganenko, and R. H. W. Friedel, AGU, Washington, D. C.

Spanswick, E., E. Donovan, R. Friedel, and A. Korth (2007), Ground based identification of dispersionless electron injections, *Geophys. Res. Lett.*, *34*, L03101, doi:10.1029/2006GL028329.

Summers, D., B. Ni, and N. P. Meredith (2007), Timescales for radiation belt electron acceleration and loss due to resonant wave-particle interactions: 2. Evaluation for VLF chorus, ELF hiss, and electromagnetic ion cyclotron waves, *J. Geophys. Res.*, *112*, A04207, doi:10.1029/2006JA011993.

Terkildsen, M. B., B. J. Fraser, F. W. Menk, and R. J. Morris (2001), Imaging riometer observations of absorption patches associated with magnetic impulse events, in *S-RAMP Proceedings of the AIP Congress, ANARE Reports No 146*, edited by R. J. Morris and P. J. Wilkinson, pp. 165–180, Aust. Antarct. Div., Tasmania, Australia.

Turunen, E., H. Matveinen, J. Tolvanen, and H. Ranta (1996), D-region ion chemistry model, in *STEP Handbook of Ionospheric Models*, edited by W. Schunk, pp. 1–25, SCOSTEP Secr., Boulder, Colo.

Vagina, L. I., and V. A. Sergeev (1996), Dynamics of the substorm current system, in *Proceedings of the Third International Conference on Substorms, ICS-3, Versailles, France*, edited by E. J. Rolfe and B. Kaldeich, p. 609, Eur. Space Agency, Paris, 12–17 May.

Wait, J. R., and K. P. Spies (1964), Characteristics of the Earth-ionosphere waveguide for VLF radio waves, *NBS Tech. Notes 300*, U.S. Dep. of Commer., Natl. Bureau of Stand., Boulder, Colo.

Zaharia, S., J. Birn, R. H. W. Friedel, G. D. Reeves, M. F. Thomsen, and C. Z. Cheng (2004), Substorm injection modeling with nondipolar, time-dependent background field, *J. Geophys. Res.*, *109*, A10211, doi:10.1029/2004JA010464.